Basin-scale development of giant collapse structures induced by gypsum diagenesis

Jimmy Moneron[*,1], and Christopher Aiden-Lee Jackson[2,3]

[1]*Department of Earth Sciences, University of Oxford, Oxford OX1 3AN, UK*

[2]*WSP UK Ltd, 8 First Street, Manchester, M15 4RP, UK*

[3]*Landscape and Basins Research Group (LBRG), Department of Earth Science and Engineering, Imperial College London, London SW7 2AZ, UK*

ABSTRACT

Across buried sedimentary basins, the dissolution-prone nature of evaporite sequences drives the formation of collapse structures (e.g., sinkholes), fundamentally transforming landscapes at large scales. Understanding where, why, and how such structures form is crucial, given they pose geological hazards that may threaten human safety and infrastructure stability, or may affect subsurface resource extraction and geological storage. Here, we use 3D seismic reflection and borehole data from the Southern North Sea Basin to document giant (km-wide and several hundred-metres deep) collapse structures within the Zechstein Supergroup (Permian) that developed at the basin-scale (>10,000km^2). Critically, these structures invariably overlie gypsum buildups capped by thick halite, with seismic-stratigraphic relationships enabling precise dating and facilitating accurate modelling. We propose that the transformation of gypsum to anhydrite during early burial initiated the extrusion of NaCl-undersaturated water, which provoked dissolution of the

capping halite, leading to collapse at the depositional surface. The resulting landscape was buried and thus preserved by a potash infilling unit. To the best of our knowledge, the basin-wide development of this type of structures has not previously been described in the stratigraphic record.

INTRODUCTION

Geomorphological depressions can form due to the subsurface dissolution of rocks, being widely documented on Earth and other planetary bodies (De Mille et al., 1964; Adams et al., 2009). In evaporitic successions, these structures form in response to chemical saturation imbalances within percolating pore fluids, more specially where NaCl-undersaturated fluids encounter highly soluble rocks such as halite. This process can create large (>10m wide and deep), areally extensive (i.e., up to several km^2), subsurface cavities evolving into collapse structures, such as sinkholes or dolines (Arkin & Gilat, 2000). These dissolution-induced structures (Hardage et al., 1996) pose significant (geo)hazards, rendering areas unstable and largely uninhabitable (Arkin & Gilat, 2000).

In addition to dissolution by undersaturated fluids, there are several other processes that may occur during early burial of evaporite-dominated sequences. For example, the transformation of gypsum ($CaSO_4 \cdot 2H_2O$) to anhydrite ($CaSO_4$) can result in substantial volume/density changes in the subsurface rock mass (Stewart, 1963). In layered evaporite sequences (LES; *sensu* Rowan et al., 2019), a variety of coupled diagenetic-dissolution-deformation processes should occur. Whereas mine or surface exposures analyses are constrained by the scale and lack of broad stratigraphic context, imaging by 3D seismic data can help determine the geometry, distribution, and genesis of salt dissolution-induced deformation. Here we use these data to study the

Zechstein Supergroup (ZSG) LES, a pan-European, Permian stratigraphic unit that records polycyclic deposition of carbonate, clastic, and evaporite rocks (Taylor, 1998). The ZSG provides an exceptional geological laboratory for studying dissolution collapse structures within LES. This is due to three key factors: (1) nearly continuous imaging by 3D seismic reflection data, (2) extensive borehole coverage, and (3) a well-established, transnational stratigraphic framework. We focus on the uppermost part of the third Zechstein cycle (i.e., the Z3k), and more specifically on the spatial and possibly genetic relationship between the diagenesis of anomalously thick zones (ATZs, Fig. 1aa', Moneron, 2025) of gypsum and overlying potash-filled depressions.

STRATIGRAPHIC FRAMEWORK

In the North Sea, the ZSG comprises five main stratigraphic units (Z1-5, Smith & Crosby, 1979; Geluk, 1999) (Figs. 1, 2; Fig. S1). The Z3 "*Leine*" cycle (Fig. S1) includes the ~50m-thick, anhydrite-dominated Z3a (*Hauptanhydrit)*, the 100–200m-thick, halite-dominated Z3h, and the K-Mg-rich Z3k potash layer, locally up to 90m thick (Smith & Crosby, 1979; Taylor, 1998). Z3a contains anomalously thick (up to ~150 m compared to a background thickness of ~45m) zones (ATZs, van Gent et al., 2011, Fig. 2D-G), interpreted as syn-depositional gypsum build-ups (Moneron, 2025). These ATZs are mapped across the South Permian Basin (Fig. 1), forming an extensive (> 100km), interconnected network of sinuous ridges and elliptical mounds, with segments extending over tens of kilometres (Fig. 1). Z3a is capped by halite (Z3h), followed by Z3k, a basin-wide K-Mg-rich unit that reflects extreme hydrological isolation and desiccation (Czapowski & Bukowski, 2010). On a broader scale, the overall thickness variability of Z3k across the basin is attributed to halokinesis (Smith and Crosby, 1979). Locally, however, spatial variations in the proportions of different K-Mg salts (e.g., sylvite, carnallite, and bischofite) are significant, likely influenced by basin physiography, diagenetic processes, and internal deformation within the unit (e.g., Raith et al., 2017). The *Roter Salzton*, a ~15m-thick, isopachous layer defining the transition to the Z4 unit (Richter-Bernburg, 1955), conformably overlies the upper Z3k sequence reflections (Fig. 2).

DATA AND METHODS

We use ~16,000km² of 3D seismic data from the Southern North Sea, the "SNS MegaSurvey" (PGS, 2015), which merges 86 individual pre-stack time-migrated reflection surveys; and the "Cavendish" survey (WesternGeco) (Fig. 1). Both datasets share comparable polarity and resolution, and are displayed with SEG "normal" polarity and zero-phase wavelets, (downward increase and decrease in acoustic impedance defined by positive (red) and negative (blue) reflections, respectively). Nineteen wells (Figs. 1, S3) were used to generate seismic-to-well ties and to analyse the lithology and stratigraphic architecture of the Z3 (Fig. S2).

*A "**Seismic-To-Well Tie And Mapping**" section is provided in the Supp. Material, outlining the workflow used to correlate seismic with borehole data.*

RESULTS

The basal unit of the Z3 sequence, Z3a, is laterally extensive and predominantly composed of anhydrite, with claystone layers (as shown in Moneron, 2025). Borehole and seismic data show that Z3a is locally defined by anomalously thick zones of anhydrite (van Gent et al., 2011; Moneron, 2025). These ATZs, (see Stratigraphic Framework), have a continuous basal reflection

(Base Z3) and an elevated, though sometimes discontinuous, upper surface (Top Z3a) (Moneron, 2025, Fig. S5b-d).

The overlying Z3h is expressed in seismic reflection data by generally continuous, sub-horizontal with locally chaotic reflections. It forms a regionally, lithologically consistent layer of massive halite with minor anhydrite inclusions (Fig. 2). Where undeformed, Z3h maintains a relatively uniform thickness, except in areas over ATZs in Z3a, where it is locally thinner due to the underlying mound topography (Fig. 2D, 2F). Critically, borehole cuttings reveal that anhydrite inclusions in Z3h are predominantly located near its basal contact with Z3a (Fig. 2), with more of these inclusions over ATZs (Fig. 2G).

Z3h halite is overlain by a base Z3k irregular surface, along which 1km-wide and 300m-deep depressions are developed (Figs. 2D, 2F). The depressions flanks dip 10-20°, and exhibit a distinct, “stepped, staircase-like” morphology (centre left of Fig. 3B), clearly truncating underlying Z3h halite (Fig. 3C-D). In map-view, the 1>10km long and 0.5-1.5km wide base-Z3k depressions are elongate, curvilinear, or sub-circular (Figs. 3B-C). Notably, they directly overlie and mimic the geometry of the underlying ATZ networks (profiles of Fig. 3, Moneron, 2025). Further analysis of borehole and seismic data confirms that the base-Z3k depressions are systematically aligned above the ATZs (Fig. 3E), with thicker Z3k sequences (113m vs. 74m in non-ATZ areas; Figs. 2, 3G, S7) overlying relatively thin Z3 halite (Z3h) and the deeper ATZs (Figs. 2C-F).

The irregular surface defining the base of Z3k is capped by regionally correlatable, sub-horizontal layers of K-Mg salts (mainly sylvite, carnallite, and polyhalite), with variable proportions of intercalated halite (Figs. 2, S2-S4). The K-Mg intra-layers (10s of m, i.e., below or at seismic resolution) are identified in cuttings, and expressed as single high-amplitude reflections, corresponding to a distinct shift to high GR values (Fig. 2G), allowing regional mapping across most studied wells.

Noteworthily, Z3k thickens by up to 250% into the base-Z3k depressions, where one or two sub-horizontal reflections in the lower half of Z3k onlap the flanks of these depressions (Fig. 3C-D, S5B-D). It is further shown that these depressions controlled the Z3k composition, with a K-Mg salt to halite ratio significantly higher within the base-Z3k depressions (i.e., above the ATZs of Z3a; Fig. 2G). Importantly, thickness and lithology variations in Z3k appear independent of the structural configuration of the underlying units (Z1-Z2 and Z3a), remaining isopachous irrespective of whether Z3a is sub-horizontal or folded (Fig. S5E-G).

INTERPRETATION AND DISCUSSION

From Gypsum Buildups To Salt Collapse

We have determined that these base Z3k depressions are not halokinesis-related features (i.e., Z3k remaining isopachous irrespective of whether Z3a is sub-horizontal or folded, Fig. S5E-G). Instead, they represent buried sinkholes (i.e., closed depressions, Waltham et al., 2005), as evidenced by the truncation of the underlying Z3h unit and the sub-horizontal, onlapping Z3k reflections above (Fig. 3C, S5B-D). A key question arising from our data is then: “Why do the base-Z3k depressions consistently align with ATZs in the Z3a anhydrite?”. Based on their spatial relationship, observations from other salt basins, and the composition of the Z3 unit, we propose that the answer may lie in diagenetic transformations during early burial.

Following ATZ accumulation and a shift in brine chemistry from gypsum to halite saturation (Fig. 4A), early burial triggered the transformation of Z3a gypsum to anhydrite (Peryt et al., 2010), releasing 30-40% of its rock volume as mineral-bound water (Langbein, 1987). Loading by overlying halite led to compaction, increased pore pressure (Fig. 4B), and hydrofracturing, a common process in overpressured, low-permeability sequences, where fluid buildup generates fracture networks that facilitate fluid escape (Cosgrove, 1995). These fractures, although too small and thus not possible to image within halite in seismic reflection data, may have provided pathways for fluid migration, inducing thermal-chemical disequilibrium, dissolution, and destabilising the overlying landscape, leading to its collapse (Fig. 4C). Fluid extrusion during gypsum diagenesis also explains the presence of anhydrite inclusions in Z3h (Fig. 2G) (Behlau & Mingerzahn, 2001). This genetic link explains why the geometries of the base-Z3k depressions (elongated and curvilinear segments, and linked at triple and quadruple junctions; Fig. 3) mimic those of the underlying Z3a anhydrite networks. While this general geometry may superficially resemble dendritic drainage patterns observed in evaporitic basins (e.g., Moneron & Gvirtzman, 2022), no discernible flow direction is observed.

The transformation of gypsum to anhydrite occurs at ≥ 40°C (Stewart, 1963; Hardie, 1967; Voigt & Freyer, 2023), which in the case of the Zechstein Basin, corresponds to an estimated burial depth of c. 300 m based on: 1) c. 100-150 ms vertical distance between the ATZs and the top Z3k (i.e., the free surface) and a halite velocity of ~4.5 km/s (see Grant et al., 2019); and 2) a surface T° of 25–35°C during Z3h deposition (e.g., Dead Sea; Sirota et al., 2017) and a geothermal gradient of 30°C/km (Gluyas et al., 2018). This also aligns with the compositional changes in the overlying Z3k attributed to Z3a gypsum dewatering (Borchert & Muir, 1964).

Impact of diagenesis-induced collapse on the Permian landscape

As described above, the base-Z3k depressions-controlled lithology variations in the Z3k sequence, with the depressions being enriched in K-Mg salt (Fig. 2). Z3h halite deposition terminated with episodic exposure of the basin floor, leading to the accumulation of the Z3k unit (Fig. 4C) (Czapowski & Bukowski, 2010; Raith et al., 2017). The stepped, staircase-like flanks of the base-Z3k depressions (centre left of Fig. 3B), resembling marine terraces that formed during sea-level fall (cf. coastline of the Dead Sea; Ghazleh & Kempe, 2009), suggest basin desiccation. Evaporation-refreshing cycles that fluctuated salinity (Krupp, 2005) led to alternating halite and K-Mg salt deposition on the depression flanks (Borchert & Muir, 1964; Raith et al., 2017). The Z4 clays, capping Z3k (Fig. 2-3), indicates re-establishment of marine conditions (Fig. 4D).

Implications

The coupled diagenetic, fluid flow, and dissolution processes suggest a framework for interpreting similar features in salt basins, both globally and in northern Europe (for example in the deeper and thus stratigraphically older Z1-2 interval studied by Głuszyński et al., 2024). For example, gypsum-rich basins, like the Dead Sea, are also deformed by sinkholes (Arkin & Gilat, 2000), which may also be caused by hypogenic evaporite dissolution, similar to the mechanisms proposed here (Bayari et al., 2009). Sedimentary basins affected by early salt tectonics, especially those containing sulphate deposits (Célini et al., 2024), may develop localised thickening within LES. These thickness variations can increase susceptibility to spatially variable, diagenesis-induced deformation. In this context, collapse may pose significant offshore geohazards, disrupting infrastructure, future drilling, pipelines, and subsurface gas storage projects. Understanding the distribution of underlying thickness variations in evaporites, is therefore critical.

CONCLUSIONS

This research highlights the role of gypsum diagenesis in shaping evaporite-bearing basins, exemplified by the Zechstein Basin. Analysis of seismic and borehole data reveals a multi-stage process where gypsum-to-anhydrite transformation releases pore water, triggering halite dissolution and forming collapse structures later infilled with potash. The alignment of depressions with gypsum mounds underscores how thickness heterogeneities influence surface stability, offering a new framework for understanding large-scale salt collapse and its global implications.

ACKNOWLEDGEMENTS

This research was carried out under the Agile Initiative–NERC grant number NE/W004976/1. We are grateful to Schlumberger for providing Petrel. B. Aldridge, D. Phillips, and J. Cartwright are thanked for engaging discussions. Mike Kendall (Head of the Department, University of Oxford) is thanked for his support in publishing this paper. Seismic (SNS MegaSurvey) and well datasets are provided by the North Sea Transition Authority and/or other third parties.

REFERENCES CITED

Adams, J. B., Gillespie, A. R., Jackson, M. P. A., Montgomery, D. R., Dooley, T. P., Combe, J.

P., & Schreiber, B. C., 2009. Salt tectonics and collapse of Hebes Chasma, Valles Marineris, Mars. *Geology*, *37*(8), 691-694.

Arkin, Y., & Gilat, A. (2000). Dead Sea sinkholes–an ever-developing hazard. *Environmental Geology*, *39*, 711-722.

Bayari, C. S., Pekkan, E., & Ozyurt, N. N., 2009. Obruks, as giant collapse dolines caused by hypogenic karstification in central Anatolia, Turkey: analysis of likely formation processes. Hydrogeology Journal, 17(2), 327.

Behlau, J., Mingerzahn, G., 2001. Geological and tectonic investigations in the former Morsleben salt mine (Germany) as a basis for the safety assessment of a radioactive waste repository. Eng. Geol. 61, 83–97. https://doi.org/10.1016/S0013-7952 (01)00038-2.

Borchert, H. & Muir, R., 1964. Salt deposits: the origin, metamorphism and deformation of evaporites. Van, D. Nostrand Company Ltd (Salzgitter).

Célini, N., Pichat, A., & Ringenbach, J. C., 2024. Salt tectonics synchronous with salt deposition in the Santos Basin (Ariri Formation, Brazil). Earth and Planetary Science Letters, 641, 118853.

Coelewij, P., Haug, G. & Van Kuijk, H. 1978. Magnesium-salt exploration in the northeastern Netherlands. Geologie en Mijnbouw 57(4): 487–502

Cosgrove, J. W., 1995. The expression of hydraulic fracturing in rocks and sediments. *Geological Society, London, Special Publications*, *92*(1), 187-196.

Czapowski, G., & Bukowski, K. (2010). Geology and resources of salt deposits in Poland: the state of the art. *Geological Quarterly*, *54*, 509-518.

De Mille, G., Shouldice, J. R., & Nelson, H. W. (1964). Collapse structures related to evaporites of the Prairie Formation, Saskatchewan. *Geological Society of America Bulletin*, *75*(4), 307-316.

Geluk, M., 1999. Late Permian (Zechstein) rifting in the Netherlands; models and implications for petroleum geology. Petroleum Geoscience, 5, 189–199.

Ghazleh, S. A., and Kempe, S., 2009, Geomorphology of Lake Lisan terraces along the eastern coast of the Dead Sea, Jordan, Geomorphology, 108, 246-263.

Gluyas, J. G., Adams, C. A., Busby, J. P., Craig, J., Hirst, C., Manning, D. A. C., ... & Younger, P. L. (2018). Keeping warm: a review of deep geothermal potential of the UK. *Proceedings of the Institution of Mechanical Engineers, Part A: Journal of Power and Energy*, *232*(1), 115-126.

Głuszyński, A., Jarosiński, M., Dąbrowski, M., & Peryt, T., 2025. Giant polygonal anhydrite ridges in the Southern Permian Basin. Geology, 53(2), 109-113.

Grant, R. J., Underhill, J. R., Hernández-Casado, J., Barker, S. M., & Jamieson, R. J. (2019). Upper Permian Zechstein Supergroup carbonate-evaporite platform palaeomorphology in the UK southern North Sea. Marine and Petroleum Geology, 100, 484-518.

Hardage, B. A., Carr, D. L., Lancaster, D. E., Simmons Jr, J. L., Elphick, R. Y., Pendleton, V. M., & Johns, R. A. (1996). 3-D seismic evidence of the effects of carbonate karst collapse on overlying clastic stratigraphy and reservoir compartmentalization. *Geophysics*, *61*(5), 1336-1350.

Hardie, L.A., 1967. The gypsum–anhydrite equilibrium at one atmosphere pressure. American Mineralogist, 52, 171–200.

Herrmann, A.G., Rühe, S., and Usdowski, E., 1997. Fluid Inc1usions: Neue Erkenntnisse über den Stoffbestand NaCI-gesättigter Meerwasserlösungen im Zechstein 3. - Kali u. Salz, 12 (4): 1 1 5-125.

Krupp, R. E. (2005). Formation and chemical evolution of magnesium chloride brines by evaporite dissolution processes—Implications for evaporite geochemistry. *Geochimica et Cosmochimica Acta*, *69*(17), 4283-4299.

Langbein, R. The Zechstein sulphates: The state of the art. in *The Zechstein Facies in Europe* (ed. Peryt, T. M.) vol. 10 143–188 (Springer-Verlag, Berlin/Heidelberg, 1987).

Moneron, J., 2025. Major heterogeneity in evaporitic depositional systems: The genesis of kilometre-scale gypsum networks in the Zechstein Basin. *Global and Planetary Change*, 104710. https://doi.org/10.1016/j.gloplacha.2025.104710

Moneron, J. and Gvirtzman, Z., 2022. Late Messinian submarine channel systems in the Levant Basin: Challenging the desiccation scenario. Geology, 50(12), pp.1366-1371.Peryt, T.M., et al., 2010. Sulphur and oxygen isotope signatures of late Permian Zechstein anhydrites, West Poland: seawater evolution and diagenetic constraints. Geological Quarterly, 54, 387–400.

Raith, A.F., Strozyk, F., Visser, J., & Urai, J.L., 2017. Evolution of rheologically heterogeneous salt structures: a case study from the NE Netherlands. Solid Earth, 7, 67–82.

Richter-Bernburg, G., 1955. Stratigraphische Glie-derung des deutschen Zechsteins. Z. dt. geol. Ges. 105, 843-54.

Rowan, M.G., Urai, J.L., Fiduk, J.C. & Kukla, P.A., 2019. Deformation of intrasalt competent layers in different modes of salt tectonics. *Solid Earth*, 10(3), pp.987-1013.

Sirota, I., Enzel, Y., & Lensky, N.G., 2017. Temperature seasonality control on modern halite layers in the Dead Sea: In situ observations. Geological Society Bulletin, 129, 1181–1194.

Smith, D. B. and Crosby, A., 1979. The regional and stratigraphical context of Zechstein 3 and 4 potash deposits in the British sector of the southern North Sea and adjoining land areas. Economic Geology, 74, 397-408.

Stewart, F. H., 1963. *Marine evaporites*. US Government Printing Office.

Taylor, J.C.M., 1998. Upper Permian—Zechstein, in: Petroleum Geology of the North Sea. John Wiley & Sons, Ltd, pp. 174–211.

van Gent, H., Urai, J.L., De Keijzer, M., 2011. The internal geometry of salt structures – A first look using 3D seismic data from the Zechstein of the Netherlands. Journal of Structural Geology, 33, 292–311.

Voigt, W., & Freyer, D. (2023). Solubility of anhydrite and gypsum at temperatures below 100 C and the gypsum-anhydrite transition temperature in aqueous solutions: a re-assessment. *Frontiers in Nuclear Engineering*, *2*, 1208582.

Waltham, T., Bell, F. G., & Culshaw, M. G. (2005). *Sinkholes and subsidence: karst and cavernous rocks in engineering and construction*. Springer Science & Business Media.

Warren, J.K., 2006. Evaporites: Sediments, Resources, and Hydrocarbons. Springer.

Williams-Stroud, S.C., & Paul, J., 1997. Initiation and growth of gypsum piercement structures in the Zechstein Basin. Journal of Structural Geology, 19, 897–907

FIGURE CAPTIONS

Fig. 1 Map showing study area, data extent, (black polygons with transparent fill—seismic surveys) and the distribution of collapse structures. The dots represent the wells colour-coded as shown in Fig. 2, located in Fig. S2. Paleogeography (inset) modified after Geluk (1999) and Taylor (1998). A chronostratigraphic chart is provided in Fig. S1. **aa'**: Cross section showing the stratigraphy of the ZSG, with evaporitic cycle units Z1-Z5 (Geluk, 1999). Salt collapse-prone areas are interpreted from underlying networks of ATZs, localised thickened Z3a (Moneron, 2025). ZSG—Zechstein Supergroup. ATZ—Anomalously Thick Zone. NPB/SPB—Northern/Southern Permian Basin. PB—Polish Basin. MNSH—Mid North Sea High. The bathymetric map is modified from emodnet.eu/. Coordinates are in degrees (UTM WGS84).

Fig. 2 A-B. Well-tied seismic sections imaging the ZSG, showing the geophysical (seismic) expression of the unit, as well as the base-Z3k collapse structures and associated ATZs (located in Fig. 1). **C-F.** Profiles showing the Z3k and its relationship to ATZs. Note the thickening of the Z3k in D and F. Anhydrite inclusions, visible in lithologic logs, are represented by pink dots. **G.** Stratigraphic correlation (datum=base Z4) through the areas shown in (C-F). Location of the 4 wells in Fig. 1, with 19 wells analysed: 13 crossing a flat base Z3k surface and 6 penetrating base Z3k depressions vertically aligned with underlying ATZs (Table of Fig. S7). The anhydrite above the RS (< 10 m) represents early Z4 gypsum deposition. Uninterpreted profiles in Fig. S8.

Fig. 3 A. Location of enlargements, ATZ networks, and cross-sections for Z3k thickness assessment. Location of inset in Fig. S3. **B-C.** Structure maps of the base Z3k, highlighting depressions and associated stratigraphic relationships. White dashed polygon in B-data gap caused by a dyke. **D.** Typical Z3k depression over an ATZ, with truncation patterns, Z3k onlaps, with metrics for measuring normalised thickness variations (in G). **E.** Thickness map of the Z3k layer. White dashed lines-ATZ network boundaries showing alignment with base-Z3k depressions. **F.** Upper inset: Dip curvature map of base-Z3k, representing the rate of change of dip in the maximum dip direction, with a 10° cutoff, (~35 ms thickness, lower inset). **G.** Normalised Z3k thickness distributions, showing a distinct thickness increase over ATZs (~30 cross sections analysed, Fig. S7). Uninterpreted profiles in Fig. S8.

Fig. 4 Four-stage conceptual model for potash-filled depressions genesis in the Zechstein Basin, expanding on gypsum buildup formation described in Moneron (2025, Fig. 10) to illustrate its later transformation via dehydration. **A**. Formation of gypsum ATZs during Z3a deposition. **B**. Burial under Z3h halite and compaction of gypsum layers. **C**. Gypsum dehydration to anhydrite releases brines, inducing halite dissolution, subsidence, and collapse. **D**. Depressions infilled with K-Mg salts during Z3k deposition, transitioning to stability with Z4 claystones. Note the effect of compaction due to burial under a uniform load of Z3h. **Insets**: Cross-sectional views of evolving topography.

FIGURES

Figure 1

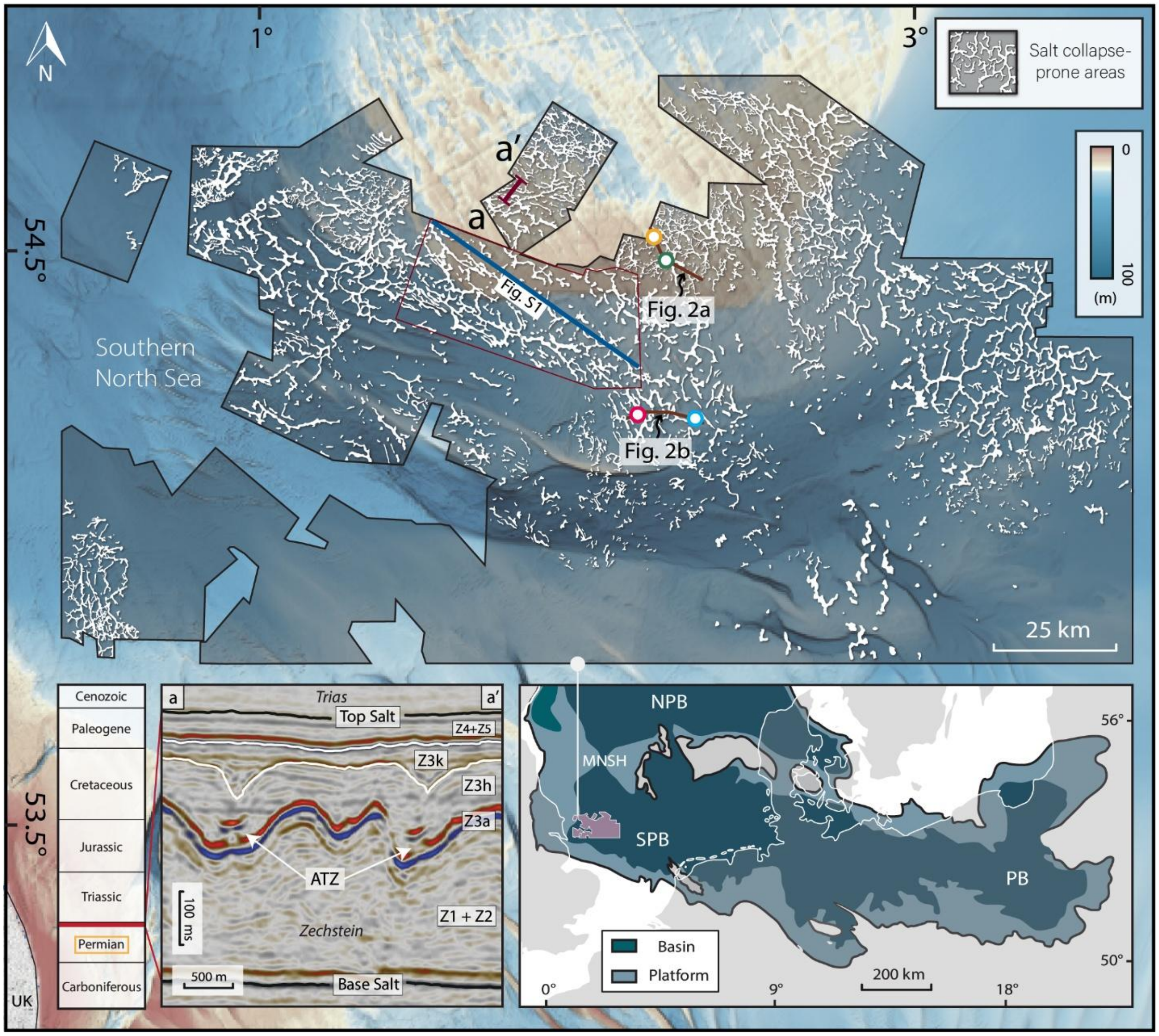

Figure 2

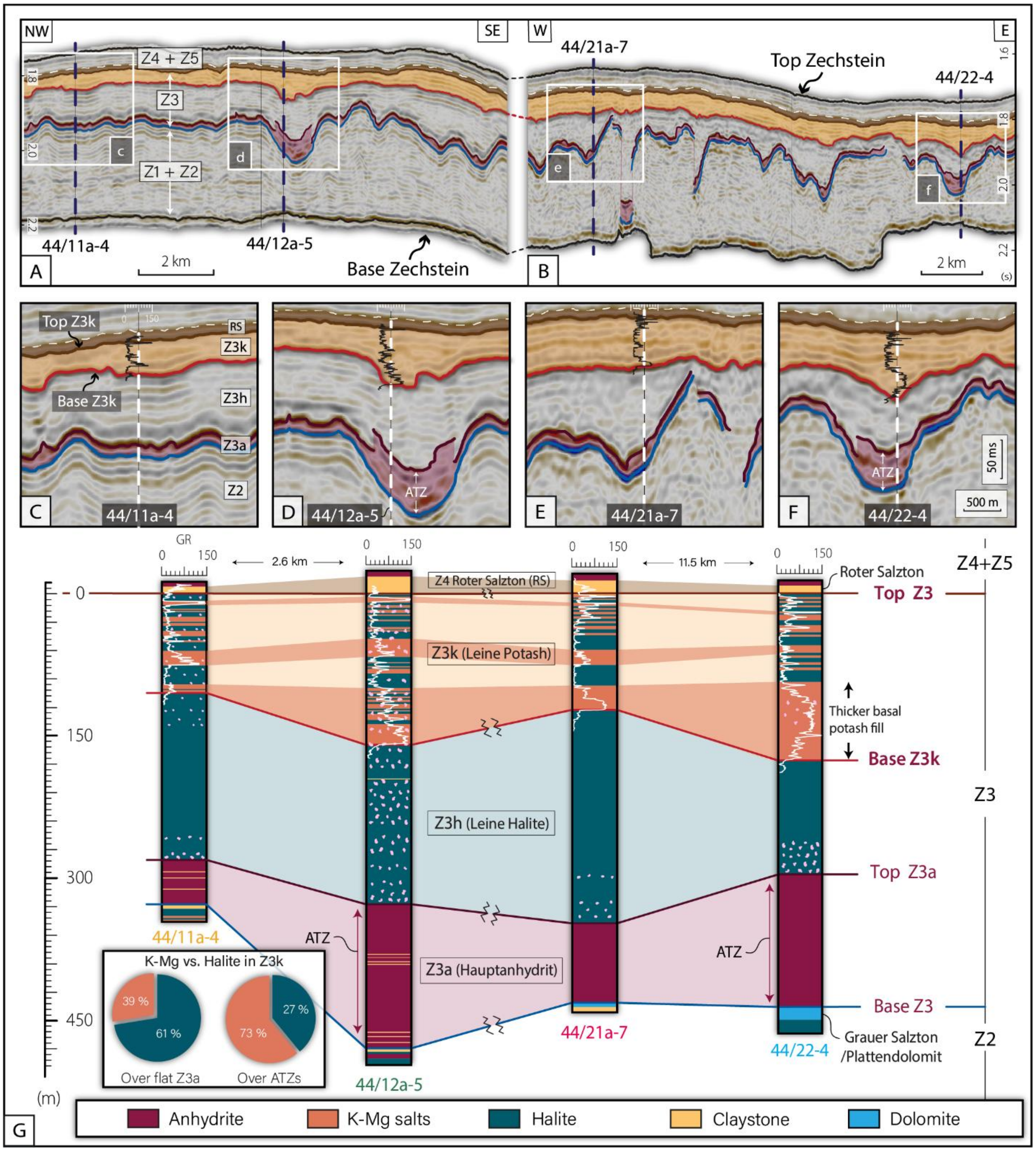

NW
SE
W
E
Z4 + Z5
Z3
Z1 + Z2
c
d
e
f
44/11a-4
44/12a-5
44/21a-7
44/22-4
Top Zechstein
Base Zechstein
2 km
A
B
(s)
Top Z3k
Base Z3k
RS
Z3k
Z3h
Z3a
Z2
ATZ
50 ms
500 m
C
D
E
F
GR
0
150
2.6 km
11.5 km
Z4 Roter Salzton (RS)
Roter Salzton
Z4+Z5
Top Z3
Z3k (Leine Potash)
Thicker basal potash fill
Base Z3k
Z3h (Leine Halite)
Z3
Top Z3a
Z3a (Hauptanhydrit)
Base Z3
Grauer Salzton /Plattendolomit
Z2
K-Mg vs. Halite in Z3k
39 %
61 %
73 %
27 %
Over flat Z3a
Over ATZs
(m)
G
Anhydrite
K-Mg salts
Halite
Claystone
Dolomite

339 **Figure 3**

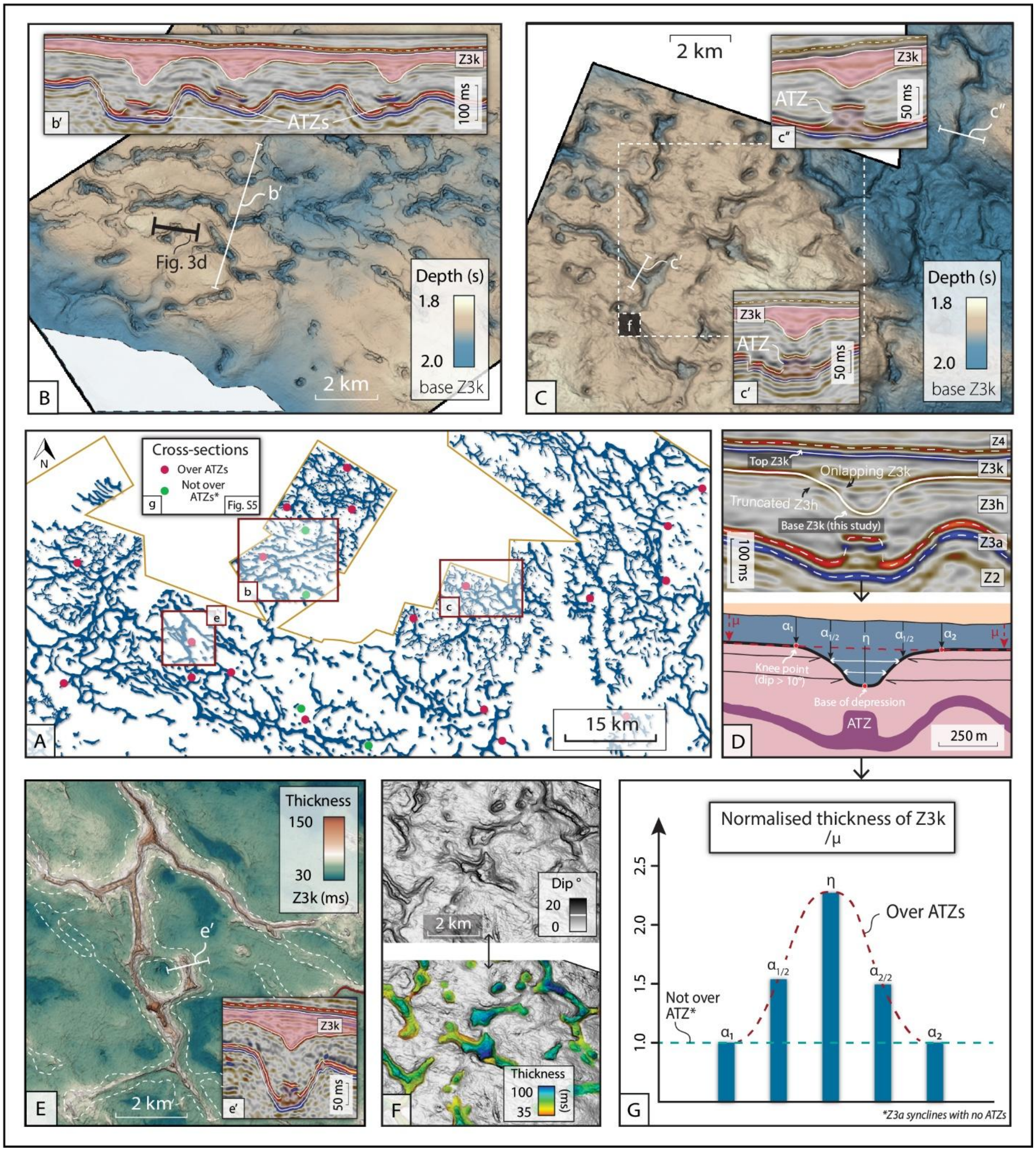

340

341

Figure 4

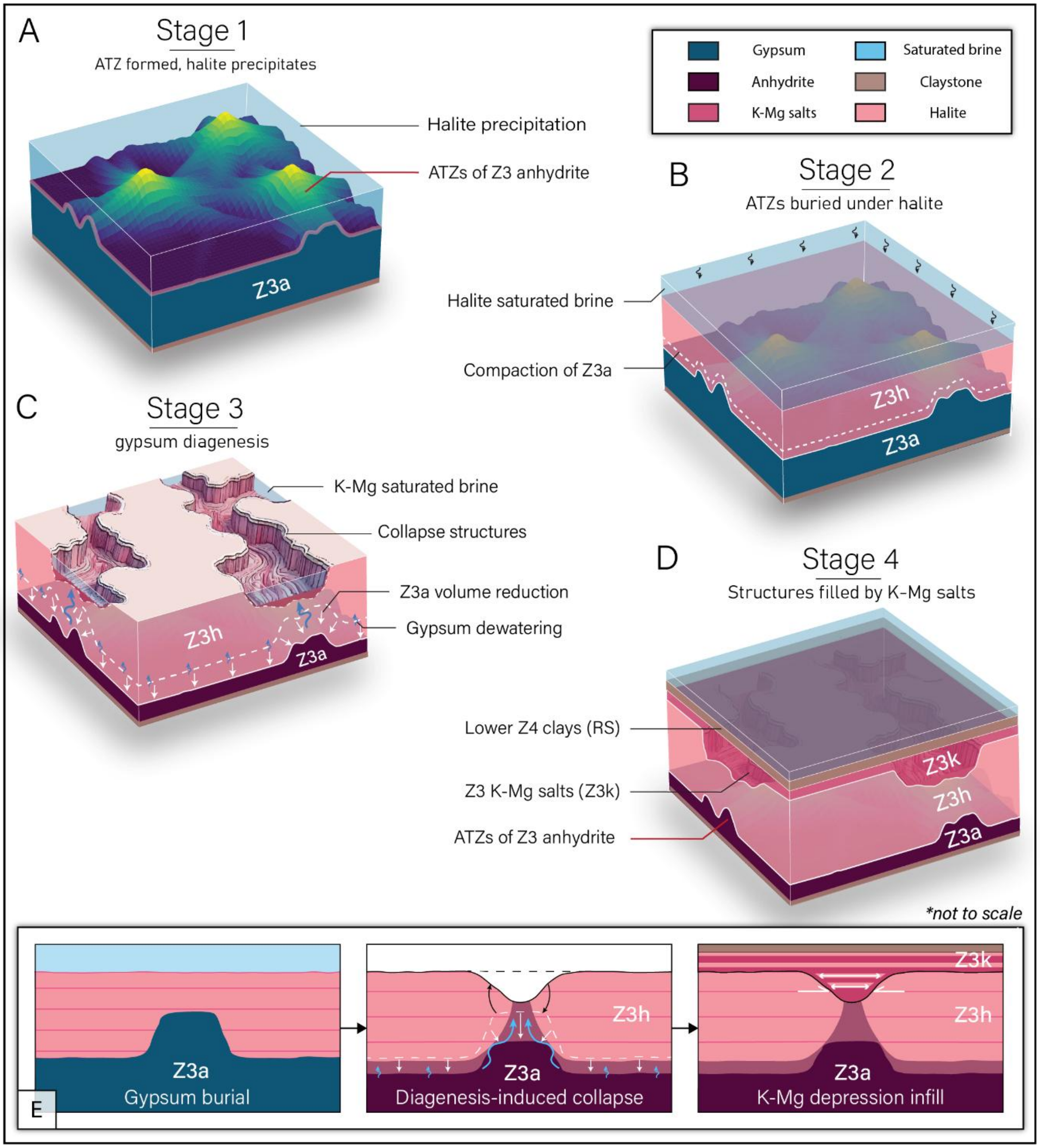

A
Stage 1
ATZ formed, halite precipitates
Halite precipitation
ATZs of Z3 anhydrite
Z3a
Gypsum
Anhydrite
K-Mg salts
Saturated brine
Claystone
Halite
B
Stage 2
ATZs buried under halite
Halite saturated brine
Compaction of Z3a
Z3h
Z3a
C
Stage 3
gypsum diagenesis
K-Mg saturated brine
Collapse structures
Z3a volume reduction
Gypsum dewatering
Z3h
Z3a
D
Stage 4
Structures filled by K-Mg salts
Lower Z4 clays (RS)
Z3 K-Mg salts (Z3k)
ATZs of Z3 anhydrite
Z3k
Z3h
Z3a
*not to scale
E
Z3a
Gypsum burial
Z3h
Z3a
Diagenesis-induced collapse
Z3k
Z3h
Z3a
K-Mg depression infill

Supplemental Material for "Basin-scale development of giant collapse structures induced by gypsum diagenesis"

Jimmy Moneron[*,1], and Christopher Aiden-Lee Jackson[2,3]

[1]*Department of Earth Sciences, University of Oxford, Oxford OX1 3AN, UK*

[2]*WSP UK Ltd, 8 First Street, Manchester, M15 4RP, UK*

[3]*Landscape and Basins Research Group (LBRG), Department of Earth Science and Engineering, Imperial College London, London SW7 2AZ, UK*

ADDITIONAL METHODS

Seismic-To-Well Tie And Mapping

We generated synthetic seismograms to tie lithological and seismic-stratigraphic boundaries interpreted from the wells and seismic data, respectively (Fig. S2). Borehole data included drilling cuttings (9m sampling frequency) and petrophysical logs (e.g., GR, DT, RHOB), which together enabled a detailed stratigraphic analysis of Z3k and mapping of its bounding seismic reflections (base and top Z3k). Seismic and well-logs show that: (1) top Z3k corresponds to a positive reflection (Fig. S2), marking the downward transition from Z4 claystone to K-Mg-rich layers, with GR logs showing values up to 150 API; and (2) base Z3k corresponds to another positive reflection (Fig. S2), corresponding to a thick Z3k K-Mg-rich layer directly overlying the halite-dominated Z3h.

Key seismic horizons identified in synthetic seismograms were mapped across the study area (Fig. S6) and interpreted on a seeded auto-tracked horizon picking from an original ~25 x 25m manual grid picking.

To analyse structural variability at the base Z3k, we applied a dip curvature extraction, which quantifies the rate of change of dip in the maximum dip direction. This method was applied to the interpreted structure map of the base Z3k, generating a black-and-white shaded relief representation that enhances local variations in surface geometry. This approach highlights collapse-induced deformation while reducing interpretation biases associated with conventional horizon displays. The seismic dataset used in this study consists of pre-stack time-migrated (PSTM) reflection data, which, despite the presence of velocity contrasts, provides high-quality imaging of key stratigraphic surfaces. While local velocity variations could introduce minor distortions, the consistency of dip curvature patterns across the dataset supports the robustness of our interpretation.

ADDITIONAL BACKGROUND

Zechstein Stratigraphy

Evaporite accumulation was strongly influenced by environmental variations, which led to the subdivision of the stratal architecture of the whole unit (e.g., Tucker, 1991; Mitchum and van Wagoner; 1991; Goodall et al., 1992). Four to five (Z1-Z5, Figure 2) main Zechstein seismo-stratigraphic cycles have been recognised and correlated across the (Taylor, 1998; Geluk, 2005; Peryt et al., 2010) and correspond to main "evaporitic cycles" (Warren, 2006), leading to a wide variety of basin-scale lithologies: shale, carbonates, sulphates, halite and K–Mg salts anhywhere in the central SPB (Figure 2) (e.g., Geluk et al., 2007: Biehl, 2014; Raith et al., 2016; Pichat, 2022). Typically, the basal unit in each cycle consists of carbonates, interbedded and then overlain by anhydrite, followed by thick deposits of halite, capped with an interbedded mixture of halite, anhydrite, and K-Mg (potash) salts (Smith, 1981; Ziegler, 1990; Taylor, 1998; Peryt et al., 2010).

In the Zechstein Group, the ratio of carbonates to evaporites declines progressively from the older cycles to the more recent ones (Taylor, 1998; Geluk, 1999) (Figure 2).

Stratigraphy Of The Z3k

The Z3 cycle follows a complete evaporitic sequence (Warren, 2006) beginning with clastic deposits, transitioning with carbonate and sulphate layers, and progressing to halite before culminating in K-Mg salts (Smith and Crosby, 1979). In this study, the upper elements of the Z3 (Z3k) unit were primarily examined as they are central to this analysis. The Z3k (Fig. 2c-g), documented mainly (1) from mining sites overlying salt structures in the southeast UK (Armstrong et al., 1951; Stewart, 1963; Smith, 1979, 1981; Talbot et al., 1982; Kemp et al., 2016), Germany (Richter-Bernburg, 1955; Herrmann and Knipping, 1993; Krupp, 2005) Poland (Podemski 1974, Dawidowski 1976, Czapowski 2006, Czapowski and bukowski 2010; Czapowski 2012) and (2) from offshore data (e.g., petrophysical logs and drill cuttings, Smith and Crosby, 1979; Pichat, 2022), is a chloride-dominated layer over the Z3 halite, and comprise mainly sylvinite, carnallite and halite with minor occurrences of anhydrite, kieserite, and bischofite (Herrmann, 1991, Kemp et al., 2016; Raith et al., 2017). The Z3k is 10m thick in marginal areas, with increasing thickness distally reaching up to 40, and even more (90 m) due to alleged halokinetic deformation (Smith and Crosby, 1979; Czapowski and bukowski 2010; Raith et al., 2017). Its formation involved primary evaporitic deposition and early diagenetic recrystallisation reflecting salinity fluctuations and basin dynamics (Krupp, 2005; Czapowski et al., 2012; Raith et al., 2017). The sporadic presence of bischofite “lakes”, /isolated depocenters in Poland (Hanczke, 1969; Krupp, 2005; Czapowski et al., 2012) and the Netherlands (Pichat, 2022), combined with the occurrence of "desiccation cracks" within the Z3k (Tomassi-Morawiec et al., 2008, 2009; Czapowski and

Bukowski, 2010; Czapowski et al., 2012; Raith et al., 2017), suggests episodic exposure and drying of the basin floor, under isolated conditions. Overlying the Z3k is the basal Z4 *Roter Salzton*, or "red salt clay" (Fig. 2; Richter-Bernburg, 1955, van Gent, 2011; Barabasch, 2019, Grant et al., 2019), a decametric, almost perfectly isopachous basinwide clay layer capping the Z3 potash traceable all over the SPB from the UK to the SE Netherlands.

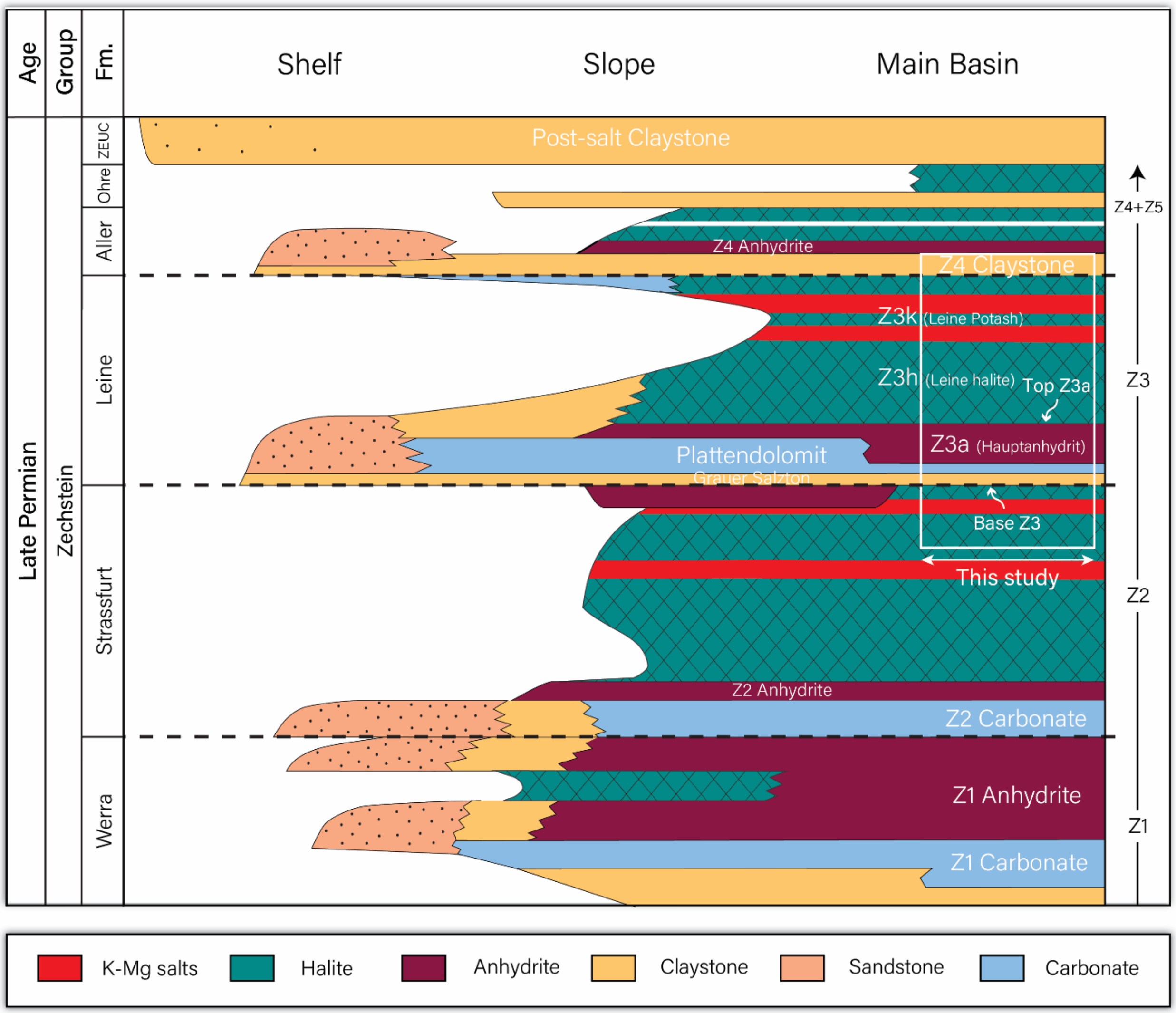

Fig. S1 Simplified lithostratigraphic chart of the Zechstein Group in the SNS. The white rectangle represents the seismo-stratigraphy of interest (see cross section aa' of Figure 1 for corresponding seismic facies). Chart modified after Geluk (1999), Geluk et al. (2007), Strozyk et al. (2014), Barabasch et al. (2019), and Pichat (2022).

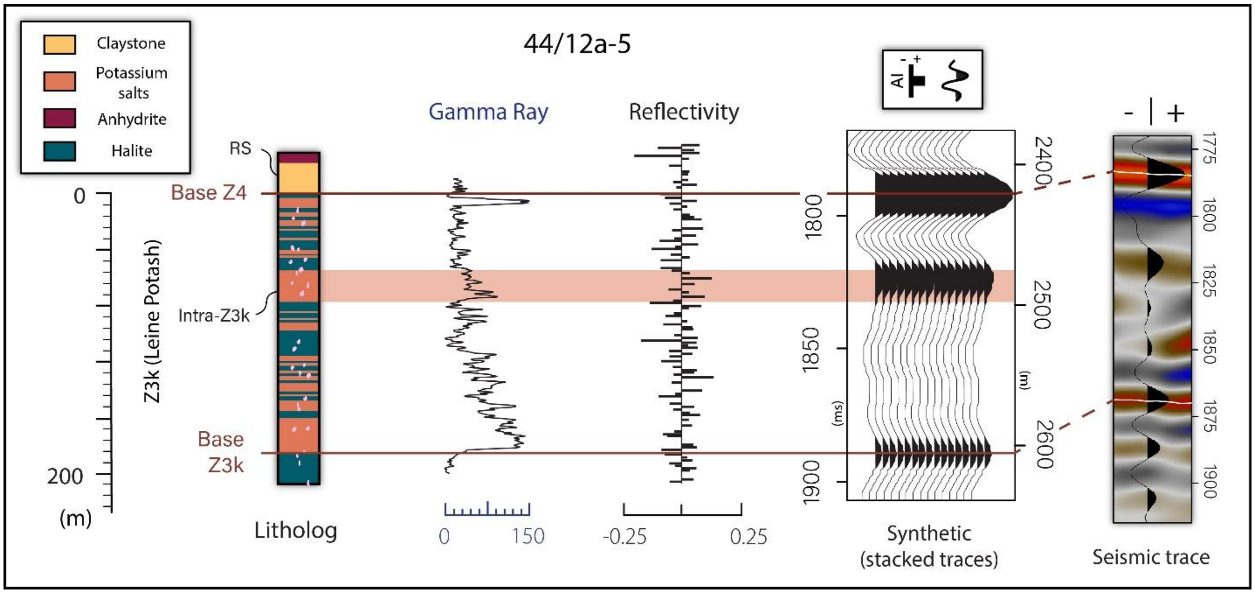

Fig. S2 Modelled synthetic seismogram, lithostratigraphy and seismic to well-tie approach for borehole 44/12a-5 (location in Figures 1 and S2). From left to right: Litholog—interpreted lithology log from drilling cuttings obtained from the mudlogging unit (vertical resolution of 9 m) and petrophysical logs. Z3a petrophysical logs: GR—Gamma Ray scaled in API units. Seismic trace over seismic data from the SNS MegaSurvey dataset. The synthetic seismogram is shown with primaries and multiples, and generated with a 1ms sample interval, the convolution of the reflectivity series is applied with a bandpass filter having a low cut of 5 Hz and a high cut of 50 Hz. The seismic wiggle measured depth (MD, two-way time, in ms) is referenced to seismic datum of mean sea level. Pink dots within litholog represent anhydrite inclusions.

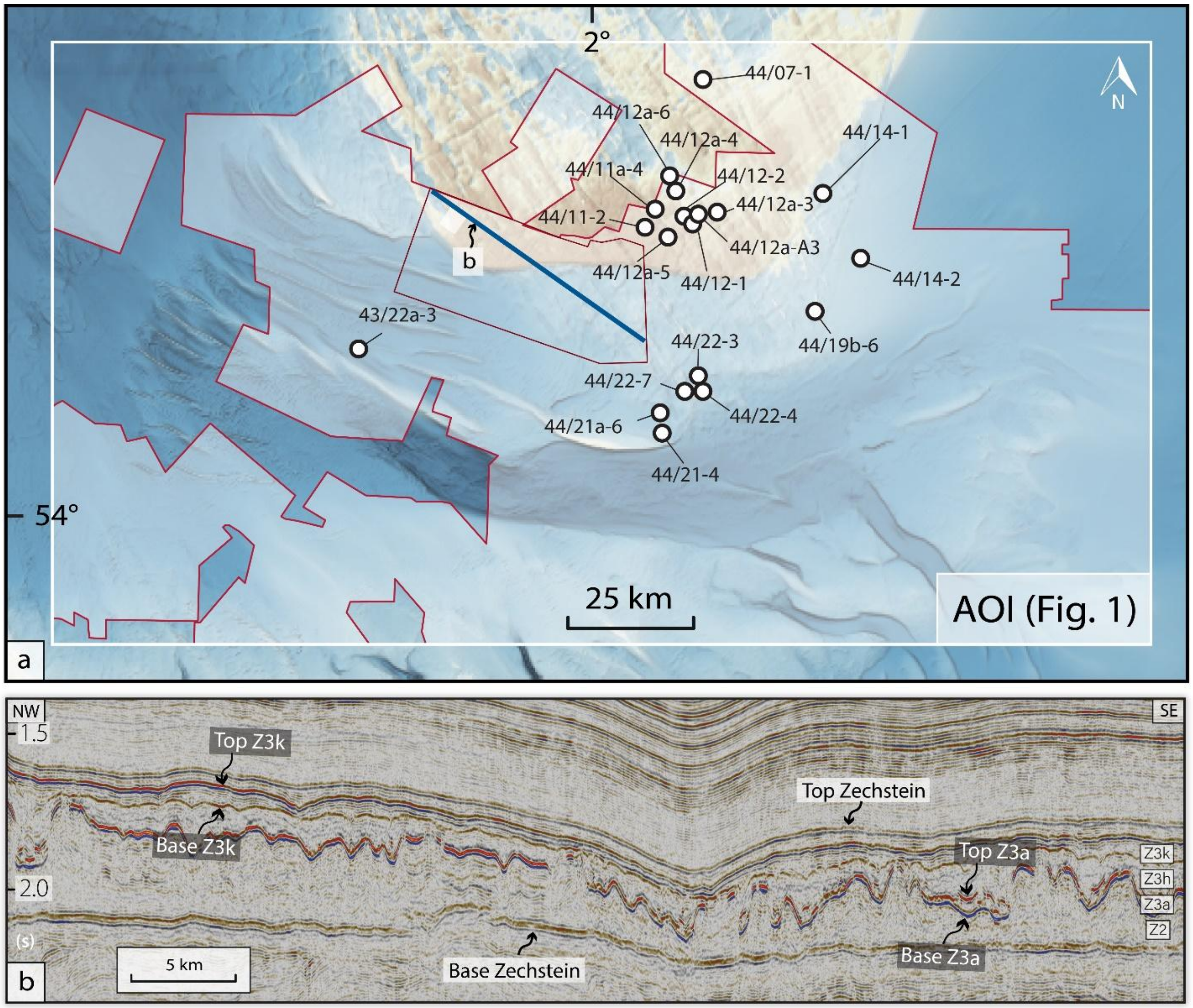

Fig. S3 a. Location of the 19 wells studied. **b**. Additional uninterpreted regional seismic reflection profile (from the Cavendish dataset, location in a.) showing how halokinetics affects the Zechstein salt. The Z3a unit appears strongly folded; and shows how the Z3k thickens due to Cenozoic deformation and salt remobilisation (e.g., Brennan et al., 2023).

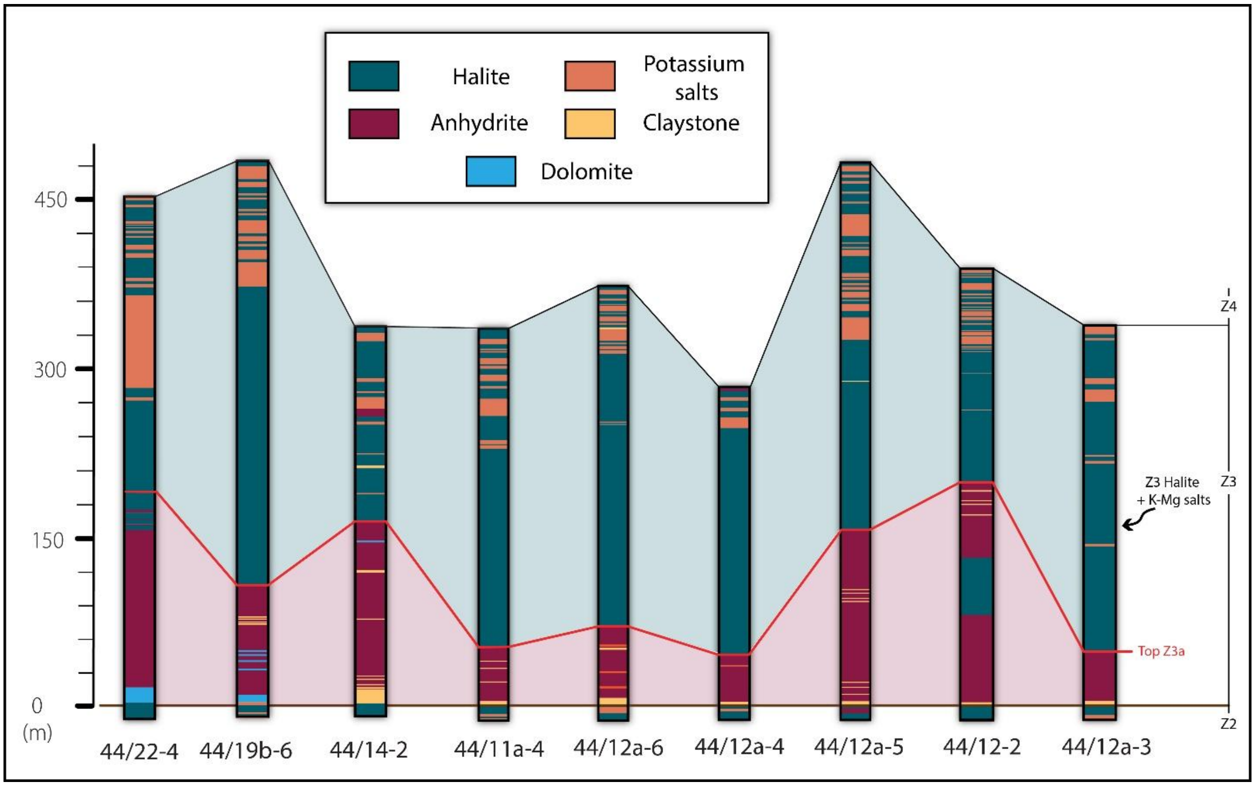

Fig. S4 Borehole additional information showing the Z3a lithology. Stratigraphic correlation (datum for correlation is defined as base Z3), derived from cuttings and petrophysical logs (obtained from https://ndr.nstauthority.co.uk/), borehole location in Figure S2.

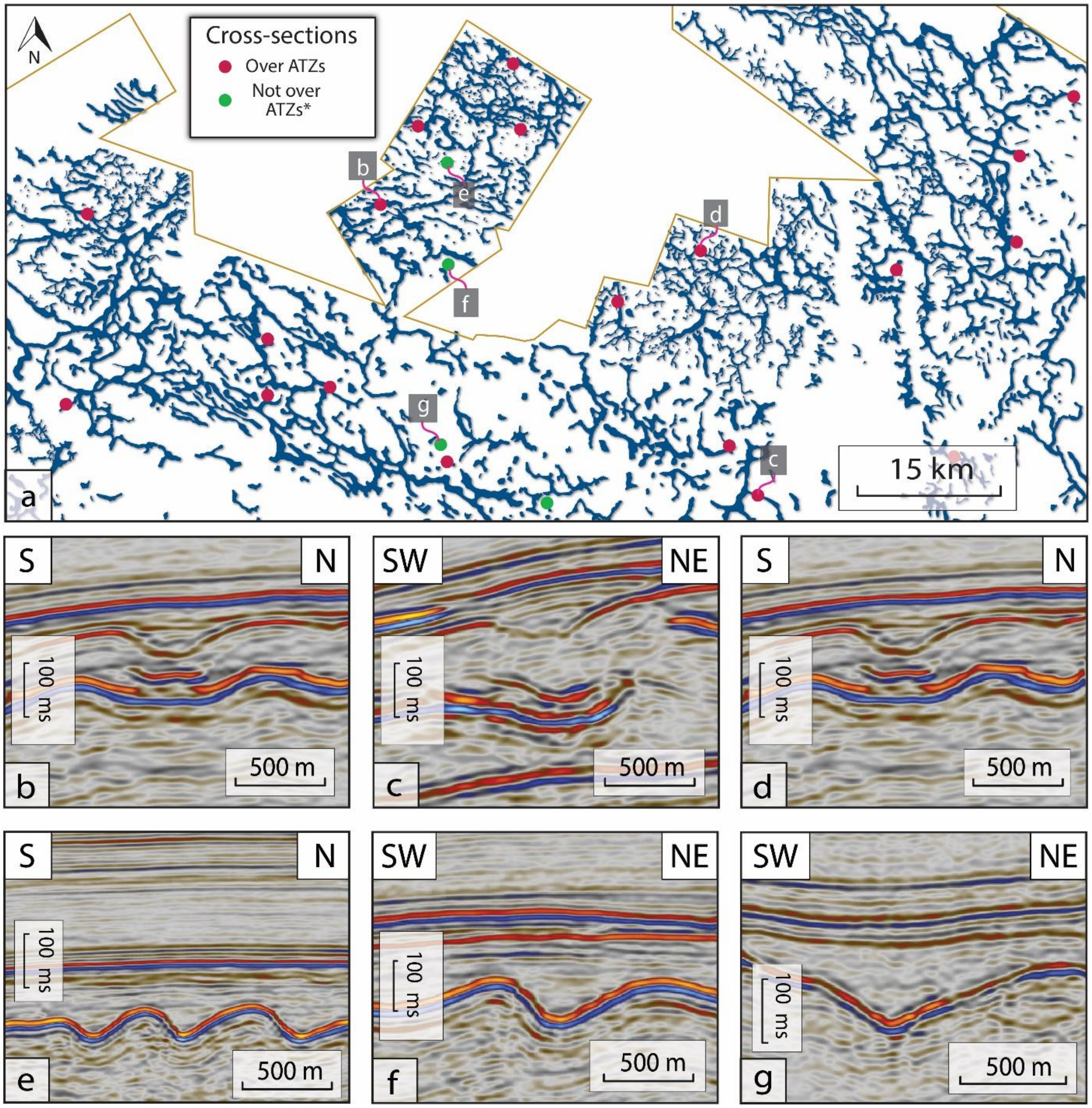

Fig. S5. Map and seismic cross-sections showing the relationship between ATZs and Z3k depressions. **b–d**. Cross-sections illustrating depressions consistently forming above ATZs. **e–g.** Cross-section showing no depressions where the Z3a lacks ATZs, even when folded.

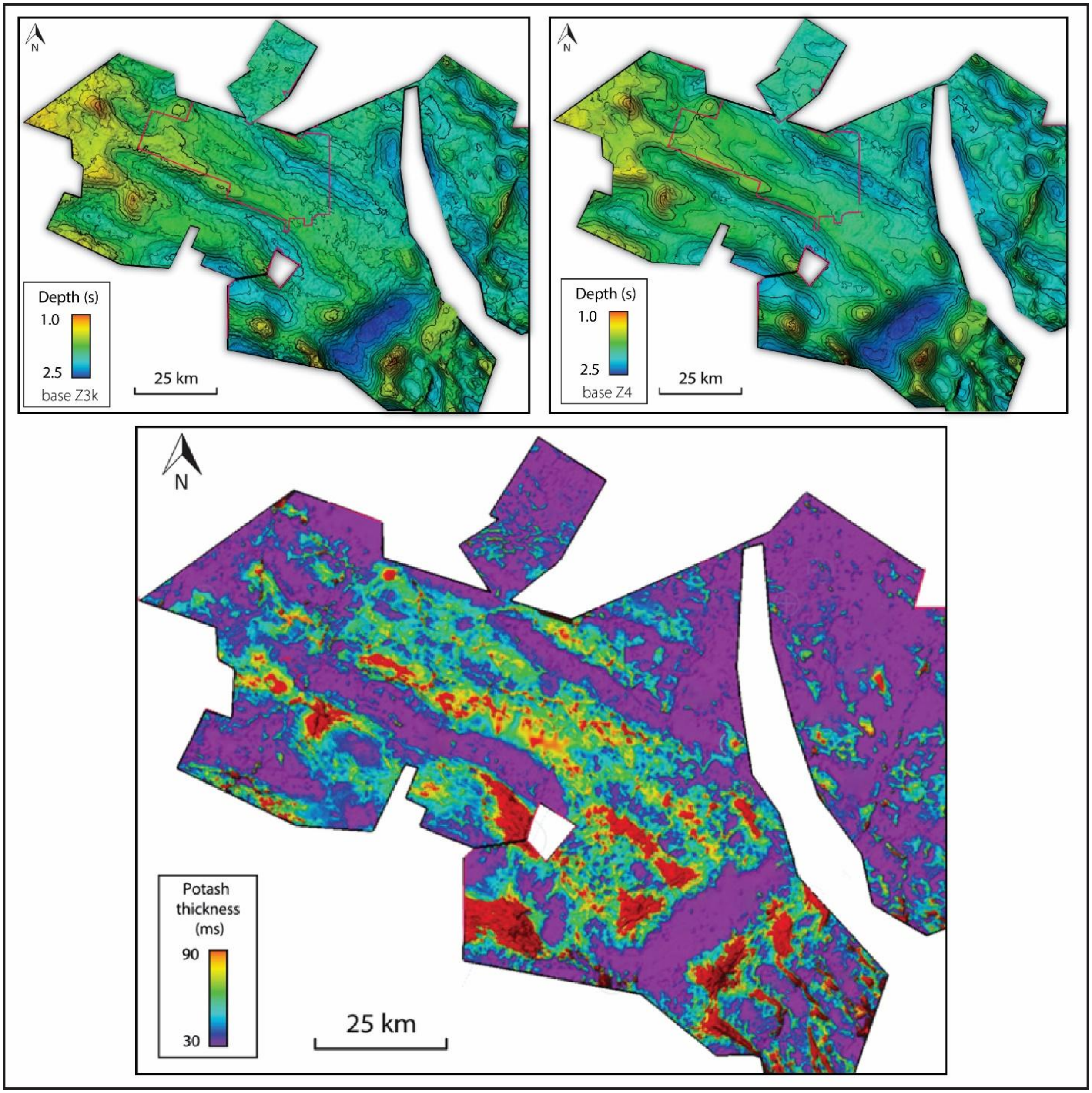

Fig. S6 Structural and thickness maps for the study area located in Fig. 1.

a

Well Number	Hauptanhydrit (ft)	Hauptanhydrit (m)	Thickness KMg (ft)	Thickness Kmg (m)	Z3k Halite (m)	Z3k total (ft)	Z3k (m)	% of Kmg Salts within Z3k
Not over ATZs								
43_22a-3	183	55.7784	100	30.48	42.672	240	73.152	41.66666667
44_07-1	180	54.864	50	15.24	64.008	260	79.248	19.23076923
44_11-2	144	43.8912	110	33.528	42.672	250	76.2	44
44_11a-4	159	48.4632	130	39.624	39.624	260	79.248	50
44_12-1	157	47.8536	40	12.192	36.576	160	48.768	25
44_12a-3	145	44.196	80	24.384	47.244	235	71.628	34.04255319
44_12a-4	143	43.5864	40	12.192	33.528	150	45.72	26.66666667
44_12a-6	202	61.5696	110	33.528	27.432	200	60.96	55
44_12a-A3	191	58.2168	155	47.244	38.1	280	85.344	55.35714286
44_14-1	138	42.0624	70	21.336	42.672	210	64.008	33.33333333
44_21-4	126.3	38.49624	110	33.528	48.768	270	82.296	40.74074074
44_21a-6	118	35.9664	150	45.72	60.96	350	106.68	42.85714286
44_22-3	143	43.5864	120	36.576	54.864	300	91.44	40
Average		47.57928	97.30769231	29.65938462	44.54769231	243.4615385	74.207077	39.06884735
Over ATZs								
44_12-2	528	160.9344	170	51.816	33.528	280	85.344	60.71428571
44_12a-5	505	153.924	350	106.68	51.816	520	158.496	67.30769231
44_14-2	481	146.6088	210	64.008	9.144	240	73.152	87.5
44/19b-6	310	94.488	190	57.912	30.48	290	88.392	65.51724138
44_22-4	470	143.256	410	124.968	39.624	540	164.592	75.92592593
44_22-7	283	86.2584	280	85.344	24.384	360	109.728	77.77777778
Average:		130.9116	268.3333333	81.788	31.496	371.6666667	113.284	72.45715385

b

	Over ATZs													
Cross section	**CS1**	**CS2**	**CS3**	**CS4**	**CS5**	**CS6**	**CS7**	**CS8**	**CS9**	**CS10**	**CS11**	**CS12**	**CS13**	**CS14**
α1	1	1	1	1	1	1	1	1	1	1	1	1	1	1
α1/2	1.3	1.25	1.77	1.2	1.35	1.4	1.46	1.4	1.5	1.22	1.7	1.3	1.2	1.8
η	3.6	1.93	2.62	1.7	1.85	2.3	2.23	1.9	2.5	1.52	2	2	1.7	2.9
α2/2	1.3	1.29	1.69	1.2	1.25	1.6	1.31	1.4	1.5	1	1.4	1.2	1.2	1.8
α2	1	1	1	1	1	1	1	1	1	1	1	1	1	1

	Over ATZs												No over ATZs					
Cross section	**CS15**	**CS16**	**CS17**	**CS18**	**CS19**	**CS20**	**CS21**	**CS22**	**CS23**	**CS24**	**CS25**	**CS26**	**CS27**	**CS29**	**CS30**	**CS31**	**CS32**	**CS33**
α1	1	1	1	1	1	1	1	1	1	1	1	1	1	1	1	1	1	1
α1/2	2.2	1.3	2.2	1.75	2.57	1.5	1.3	1.5	1.25	1.4	1.54	1.7	1.36	1	1	1	1	1
η	2.5	2	2.9	2.375	4.86	2.3	1.6	1.95	1.67	2	2.08	2.4	1.91	1	1	1	1	1
α2/2	1.5	1.1	1.7	1.625	2.71	1.6	1.4	1.55	1.33	1.5	1.69	1.8	1.55	1	1	1	1	1
α2	1	1	1	1	1	1	1	1	1	1	1	1	1	1	1	1	1	1

Fig. S7 Summary of metrics used in this study. **A**. Tabulated data comparing the thicknesses of Hauptanhydrit (Z3a), K-Mg salts, and halite (Z3h) within and outside ATZs. Averaged thicknesses and proportions of K-Mg salts within the Z3k unit are also provided, highlighting significant differences between areas overlying ATZs and those that do not. **B**. Cross-section indices categorising sections over and outside ATZs, indicating the distribution and structural variability across study regions.

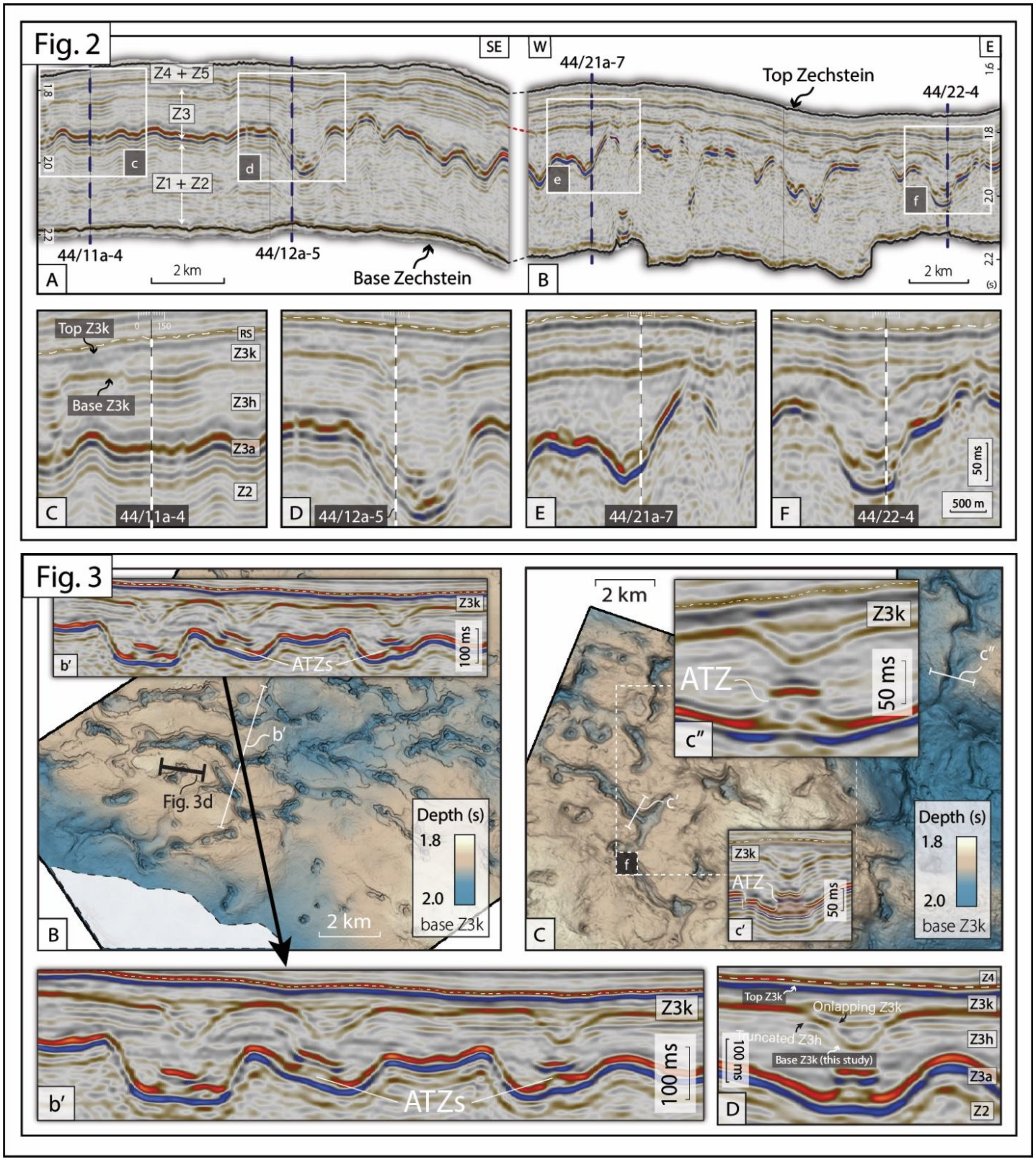

Fig. S8. uninterpreted profiles of Figs. 2 and 3.

ADDITIONAL REFERENCES CITED

Armstrong, G., Dunham, K. C., Harvey, C. O., Sabine, P. A., & Waters, W. F. (1951). The paragenesis of sylvine, carnallite, polyhalite, and kieserite in eskdale borings nos. 3, 4, and 6, north-east yorkshire. Mineralogical magazine and journal of the Mineralogical Society, 29(214), 667-689.

Barabasch, J., Urai, J.L., Raith, A.F., and De Jager, J., 2019. The early life of a salt giant: 3D seismic study on syntectonic Zechstein salt and stringer deposition on the Friesland Platform, Netherlands. Z. Dtsch. Ges. Für Geowiss., 170, 273–288. https://doi.org/10.1127/zdgg/2019/0186.

Biehl, B.C., Reuning, L., Strozyk, F., and Kukla, P.A., 2014. Origin and deformation of intra-salt sulphate layers: an example from the Dutch Zechstein (Late Permian). International Journal of Earth Sciences, 103, 697–712. https://doi.org/10.1007/s00531-014-0999-4.

Bornemann, O., 1991. Zur Geologie des Salzstocks Gorleben nach den Bohrergebnissen. - BfS-Schriften, 4: 1-67; Salzgitter.

Brennan, C., Preiss, A., and Adam, J., 2023. Three-dimensional seismic classification of salt structure morphologies across the Southern North Sea. AAPG Bulletin, 107(12), 2141–2167.

Czapowski G., 2006. Permskie sole potasowo-magnezowe na obszarze centralnej i poludniowo-zachodniej Polski – obecny stan rozpoznania. Przeglad Geologiczny, 54, 4, 317.

Czapowski, G., and Bukowski, G., 2010. Halokinetic impact on Zechstein salt deposition. Geological Quarterly, 54, 20–36.

Czapowski, G., Tomassi-Morawiec, H., Toboła, T., & Tadych, T. (2012). Geology, geochemistry and petrological characteristics of potash salt units from PZ2 and PZ3 Zechstein (Late Permian) cycles in Poland. *Geol. Geophys. Environ*, *38*(2), 153-188.

Dawidowski S., 1976. Obecne rozpoznanie koncentracji soli potasowych mlodszych (K3) w okolicy Nowej Soli i perspektywy ich gospodarczego zastosowania. *Przeglad Geologiczny*, 24, 9, 545–546.

Hanczke T., 1969. Mineralogia i petrogra□ a soli cechsztynskich kopalni Klodawa. *Prace Muzeum Ziemi*, 16, 3–52.

Herrmann, A. G., & Borstel, L. (1991). The composition and origin of fluid inclusions in Zechstein evaporites of Germany. *Neues Jahrbuch für Mineralogie Monatshefte*, (6), 263-269.

Geluk, M., 1999. Late Permian (Zechstein) rifting in the Netherlands; models and implications for petroleum geology. Pet. Geosci. 5, 189–199. https://doi.org/10.1144/petgeo.5.2.189.

Geluk, M.C., 2005. Stratigraphy and Tectonics of Permo-Triassic Basins in the Netherlands and Surrounding Areas. PhD thesis, Utrecht University, Utrecht, The Netherlands.

Geluk, M.C., Wong, T.E., Batjes, D.A.J., and De Jager, J., 2007. Permian. Geology of the Netherlands, 63–83.

Goodall, I.G.; Harwood, G.M.; Kendall, A.C.; McKie, T.; Tucker, M.E., 1992. Discussion on sequence stratigraphy of carbonate-evaporite basins: Models and application to the Upper Permian (Zechstein) of northeast England and adjoining North Sea. J. Geol. Soc. 149, 1050–1054.

Grant, R.J., Underhill, J.R., Hernández-Casado, J., Barker, S.M., and Jamieson, R.J., 2019. Upper Permian Zechstein Supergroup carbonate-evaporite platform palaeomorphology in the UK southern North Sea. Marine and Petroleum Geology, 100, 484–518.

Herrmann, A. G., & Knipping, B., 1993. Waste disposal and evaporites: contributions to long-term safety (Vol. 45). Springer-Verlag.

Kemp, S. J., Smith, F. W., Wagner, D., Mounteney, I., Bell, C. P., Milne, C. J., ... & Pottas, T. L. (2016). An improved approach to characterize potash-bearing evaporite deposits, evidenced in North Yorkshire, United Kingdom. Economic Geology, 111(3), 719-742.

Krupp, R. E., 2005. Formation and chemical evolution of magnesium chloride brines by evaporite dissolution processes—Implications for evaporite geochemistry. Geochimica et Cosmochimica Acta, 69(17), 4283-4299.

Mitchum Jr, R.M. and van Wagoner, J.C., 1991. High-frequency sequences and their stacking patterns: sequence-stratigraphic evidence of high-frequency eustatic cycles. Sedimentary geology, 70(2-4), pp.131-160.

Peryt, T.M., Halas, S., and Petrivna Hryniv, S., 2010. Sulphur and oxygen isotope signatures of late Permian Zechstein anhydrites, West Poland: seawater evolution and diagenetic constraints. Geological Quarterly, 54(4), 387–400.

Pichat, A., 2022. Stratigraphy, paleogeography, and depositional setting of the K–Mg salts in the Zechstein Group of the Netherlands—Implications for the development of salt caverns. Minerals, 12(4), 486.

Podemski M., 1974. Stratygrafia a utworów cechsztynskich zachodniej czesci niecki pónocno-sudeckiej. Kwartalnik Geologiczny, 18, 4, 729–748.

Raith, A.F., Strozyk, F., Visser, J., and Urai, J.L., 2016. Evolution of rheologically heterogeneous salt structures: a case study from the NE Netherlands. Solid Earth, 7(1), 67–82. https://doi.org/10.5194/se-7-67-2016.

Raith, A.F., Strozyk, F., Visser, J., & Urai, J.L., 2017. Evolution of rheologically heterogeneous salt structures: a case study from the NE Netherlands. Solid Earth, 7, 67–82.

Richter-Bernburg, G., 1955. Stratigraphische Gliederung des deutschen Zechsteins. Z. dt. geol.

Ges. 105, 843–854.

Smith, D.B., and Crosby, A., 1979. The regional and stratigraphical context of Zechstein 3 and 4 potash deposits in the British sector of the southern North Sea and adjoining land areas. Economic Geology, 74, 397–408.

Smith, D.B., 1979. Rapid marine transgressions and regressions of the upper Permian Zechstein Sea. J. Geol. Soc. 136, 155–156. https://doi.org/10.1144/gsjgs.136.2.0155.

Smith, D.B., 1981. The evolution of the English Zechstein basin.

Stewart, F. H., 1963. *Marine evaporites*. US Government Printing Office.

Strozyk, F., Urai, J.L., van Gent, H., De Keijzer, M., Kukla, P.A., 2014. Regional variations in the structure of the Permian Zechstein 3 intrasalt stringer in the northern Netherlands: 3D seismic interpretation and implications for salt tectonic evolution. Interpretation 2, SM101–SM117. https://doi.org/10.1190/INT-2014-0037.1.

Talbot, C. J., Tully, C. P., & Woods, P. J. E. (1982). The structural geology of Boulby (potash) mine, Cleveland, United Kingdom. Tectonophysics, 85(3-4), 167-204.

Taylor, J.C.M., 1998. Upper Permian—Zechstein, in: Petroleum Geology of the North Sea. John Wiley & Sons, Ltd, pp. 174–211. https://doi.org/10.1002/9781444313413.ch6.

Tomassi-Morawiec H., Czapowski G. & Sztyrak T., 2008b. Opróbowanie geochemiczne rdzeni z utworów solnych cechsztynu w otworach wiertniczych G-34, G-39 i G-16 zlokalizowanych w KS i PMTiP „Góra”. Archiwum IKS Solino SA, Inowroclaw.

Tomassi-Morawiec H., Czapowski G., Bornemann O., Schramm M. & Misiek G., 2009. Wzorcowe profile bromowe dla solnych utworów cechsztynu w Polsce. *Gospodarka Surowcami Mineralnymi*, 25, 2, 75–143.

Tucker, M.E., 1991. Sequence stratigraphy of carbonate-evaporite basins: models and application to the Upper Permian (Zechstein) of northeast England and adjoining North Sea. J. Geol. Soc. 148, 1019–1036. https://doi.org/10.1144/gsjgs.148.6.1019.

Warren, J.K., 2006. Evaporites: Sediments, Resources and Hydrocarbons. Springer, Berlin, Heidelberg. https://doi.org/10.1007/3-540-32344-9.

Ziegler, P.A., 1990. Geological atlas of western and central Europe (Vol. 52). The Hague: Shell Internationale Petroleum Maatschappij BV.